

<https://doi.org/10.1038/s41528-024-00301-7>

Ultra-sensitive, highly linear, and hysteresis-free strain sensors enabled by gradient stiffness sliding strategy

Check for updates

Fuhua Xue¹, Qingyu Peng¹ , Renjie Ding¹, Pengyang Li¹, Xu Zhao¹, Haowen Zheng¹, Liangliang Xu¹, Zhihong Tang¹, Xinxing Zhang² & Xiaodong He¹

Developing strain sensors with both high sensitivity and high linearity has always been the goal of researchers. Compared to resistive strain sensors, capacitive strain sensors have incomparable linearity advantages, but have always been limited by low sensitivity. Here, we report a gradient stiffness sliding design strategy that addresses this problem, significantly improving sensitivity while maintaining high linearity. By controlling the distribution of the locally enhanced electric field and the heterogeneous deformation of the substrate, a strain sensor with excellent performance is successfully prepared, exhibiting a giant gauge factor (9.1×10^6) and linearity ($R^2 = 0.9997$) over the entire sensing range, together with almost no hysteresis and fast response time (17 ms). The gradient stiffness sliding design is a general strategy expected to be applied to other types of sensors to achieve ultra-high sensitivity and ultra-high linearity at the same time.

Flexible sensors overcome the disadvantages of bad biocompatibility and narrow sensing ranges of conventional rigid sensor devices and have significant practical value in artificial intelligence^{1–3}, electronic skins^{4–6}, and health monitoring^{7–9}. Developing an ideal flexible strain sensor with high sensitivity and linearity over a broad range has always been a crucial and necessary subject. Flexible strain sensors can be generally divided into three categories based on their operating mechanism: piezoelectric^{9,10}, resistive^{11–13}, and capacitive^{14,15}. Piezoelectric-type strain sensors have a fast response time to dynamic deformation and require no additional power supply, but they are incapable of detecting static loads¹⁶. Resistive-type strain sensors are capable of achieving high sensitivities, which are currently the most studied sensors¹⁷. Despite the fact that they can exhibit outstanding gauge factors (GFs) through some delicate design^{18,19}, most resistive-type strain sensors exhibit a nonlinear strain response and hysteresis effect. The real practical operation typically cannot guarantee that the installation status of the flexible strain sensor is strain-free when placing it on a sensing target, such as human skin. In this case, nonlinearity will result in significant measurement errors^{20,21}, making the calibration procedure complex and challenging. The high hysteresis effect will lead the sensor to display various results even when subjected to the same strain during loading and unloading, which is also a serious issue²². Capacitive-type strain sensors can well meet the above linearity and hysteresis requirements²³. Under the

application of uniaxial strain to conventional parallel-plate capacitive strain sensors, the facing area and the thickness of the dielectric vary synergistically due to the Poisson effect, resulting in a linear change in capacitance with strain. Although capacitive-type strain sensors have the intrinsic advantage of linearity, they suffer from the limitation of low sensitivity where the theoretical best GF that can be achieved is 1 (Supplementary Fig. 1), which is much lower than that of the resistive-type sensors¹⁴. Therefore, it is urgent to break the limitation of the low sensitivity of capacitive-type strain sensors to fulfill the demand for both a wide range of linearity and high sensitivity, which is highly desired but remains a great challenge.

Stretchable strain sensors typically consist of two components: active materials and an elastic substrate. To address the issue of sensitivity, most of the research focuses on the design and optimization of active materials^{24,25}. However, the strain sensor is a mechanical device, and strain is the most fundamental factor. Therefore, from the perspective of the mechanical structure design of the substrate, significant achievements can usually be realized^{26–30}. Chen and colleagues incorporated auxetic mechanical metamaterials with negative structural Poisson's ratio effect into the substrate structure of strain sensors. Strain signals were collected at both ends of the substrate and acted on the active material region in the middle of the substrate, resulting in a 24-fold increase in sensitivity compared to conventional structures³¹. Liu and colleagues proposed a nacre-inspired

¹National Key Laboratory of Science and Technology on Advanced Composites in Special Environments, Center for Composite Materials and Structures, Harbin Institute of Technology, 150080 Harbin, China. ²State Key Laboratory of Polymer Materials Engineering, Polymer Research Institute, Sichuan University, 610065 Chengdu, China. e-mail: pengqingyu@hit.edu.cn; xxzwwh@scu.edu.cn; hexd@hit.edu.cn

architecture composed of high-stiffness Cr cells as ‘bricks’ and stretchable strain-sensitive Ag film as ‘mortar’. High-stiffness Cr cells locally modulated the strain distribution, which avoided premature cut-through cracks and created crack-free regions during strain, achieving 2 orders of magnitude of sensitivity amplification³². However, the structure of most of the current capacitive strain sensors is parallel-plate type, which inherently limits the development of the sensitivity^{14,33,34}. Shintake et al. integrated a hierarchical auxetic structure with negative Poisson’s ratio effect into a capacitive strain sensor³⁵, resulting in a GF of 1.61, which breaks through the theoretical limit of capacitive sensors with a maximum sensitivity of 1. Someya and colleagues created a high degree of freedom in the out-of-plane direction by introducing the wrinkled structure on the electrodes³⁶, thus achieving a GF slightly above 3. Nesser et al. constructed a parallel-plate structure of ‘fragmented electrode—dielectric elastomer—fragmented electrode’, which utilizes the significant change in resistance of the electrodes during stretching to make the sensor behave as a transmission line³⁷. The strain-dependent voltage attenuation over the structure length results in a large variation of the effective capacitance (GF exceeding 37 at 3% strain). Tremendous efforts have been made to enhance sensitivity, but it is difficult to achieve a remarkable improvement^{15,38,39}.

In this study, from the perspective of structural design, we propose a capacitive strain sensor design strategy, the ‘Gradient Stiffness Sliding’ (GSS) method, which fundamentally breaks the theoretical limit of the highest sensitivity of 1. By controlling the distribution of the locally enhanced electric field and the heterogeneous deformation of the substrate, a strain sensor with excellent performance was successfully prepared, exhibiting an ultra-high sensitivity and ultra-high linearity over the entire sensing range, together with almost no hysteresis and fast response time. In addition, the GSS method can be further applied to the design of other types of flexible sensors in a promising way.

Results and discussion

Principles of GSS design strategy

In contrast to a homogeneous material, the deformation distribution of the thin film with the gradient stiffness structure can be remarkably modulated under uniaxial tensile loading (Fig. 1a). The soft part is greatly elongated,

while the hard part hardly deforms. When two such gradient stiffness films are placed head-to-tail and subjected to uniaxial tension, the facing area of the two soft parts will increase with the increase of strain (Fig. 1b). The greater the difference in stiffness between the soft part and the hard part, the larger the facing area under the same strain (Supplementary Fig. 2). This phenomenon suggests that heterogeneous deformation can be used to develop and improve the sensing performance of capacitive strain sensors. First, the half area of flexible polyvinyl chloride (PVC) film is covered, and only the other half area is treated with plasma (Fig. 1c). The PDMS layer is then cast onto the plasma-treated area, and the PDMS layer can be firmly bonded to the PVC layer due to the activated PVC surface⁴⁰. Then, before the PDMS layer is completely cured, Ecoflex is cast onto the untreated PVC area, so that the Ecoflex part and PDMS part are fused and cured at the splice to form a whole film. The Ecoflex layer and PVC layer are unbonded due to the unactivated PVC surface, so they can separate easily and slide against each other. So far, the hard PDMS/PVC part and the soft Ecoflex part form a gradient stiffness substrate (Supplementary Figs. 3 and 4). Then stick a flexible electrode on the other side of the PVC layer corresponding to the Ecoflex part. An ionic layer of polyacrylamide (PAM)/LiCl is further cast on the electrode. As a result, a PDMS/PVC-Ecoflex gradient stiffness layer with only the electrode and another gradient stiffness layer covered with an ionic layer on the electrode is assembled head to tail to form a capacitive strain sensor.

When the strain sensor is subjected to uniaxial tension^{29,31}, only the soft parts (Ecoflex parts) in the upper and lower gradient stiffness layers deform (Fig. 1d), resulting in a gradually increasing contact area between the upper electrode and the ionic layer (the lower electrode is always in full contact with the ionic layer). The increase in contact area leads to an increase in specific capacitance due to the formation of electric double layers (EDLs) at the ionic layer/electrode interface, which is about 5–6 orders of magnitude higher than its non-iontronic counterparts. There are a large number of positive and negative ion pairs distributed in the ionic layer. When the voltage is applied, electrons on the electrode and the positive ions in the ionic layer accumulate and attract to each other within the contact area at a nanometer distance, which leads to an ultra-high specific capacitance⁴¹. Theoretically, the contact area between the upper electrode and the ionic

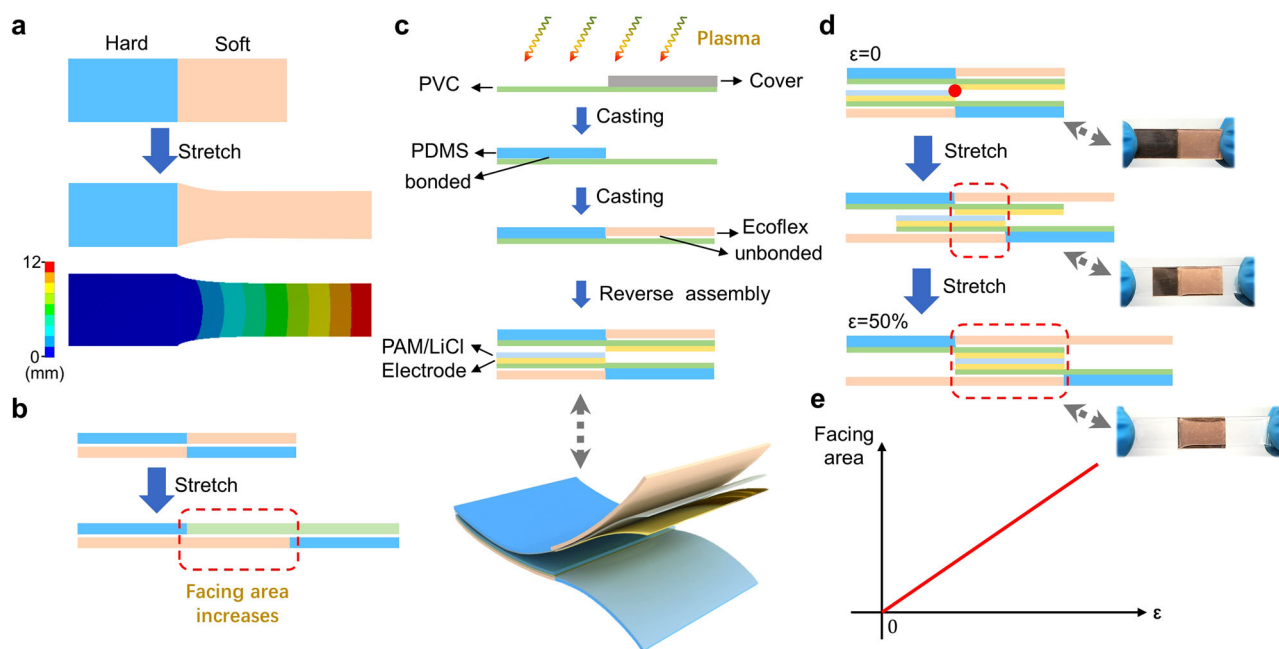


Fig. 1 | Principles of GSS design strategy. **a** The deformation distribution of the thin film with the gradient stiffness structure. **b** Schematic illustration of the change of facing area of the soft parts of two gradient stiffness layers under stretching. **c** Schematic illustration of the preparation of the GSS-designed iontronic strain

sensor. **d** Schematic illustration of the gradually increasing contact area between the upper electrode and the ionic layer under stretching. **e** The theoretical relationship between the facing area and the strain applied to the sensor.

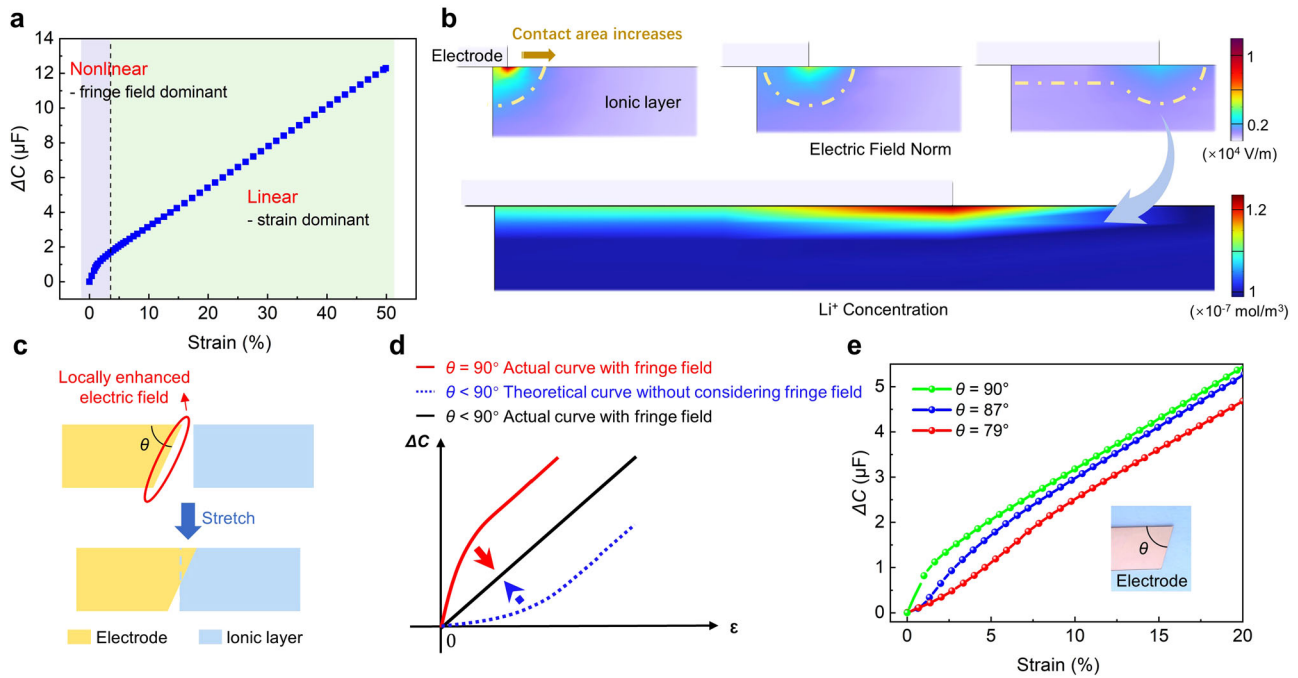


Fig. 2 | Mechanism analysis and optimization of fringe field effect. **a** The relationship between capacitance change and strain under uniaxial tension. **b** The variation of electric field norm and lithium-ion concentration distribution with the increase of the contact area between the upper electrode and the ionic layer. **c** The shape of the upper electrode was set as a trapezoid with an angle of θ . **d** Schematic

diagram of the relationship between capacitance change and strain when $\theta = 90^\circ$ (considering fringe field), $\theta < 90^\circ$ (not considering fringe field), and $\theta < 90^\circ$ (considering fringe field). **e** The relationship between capacitance change and strain when θ is equal to different angles. The inset is a photograph of a trapezoid electrode.

layer increases linearly with the strain applied to the sensor (Fig. 1e and Supplementary Fig. 5). This is also proved by finite-element simulation (Supplementary Fig. 6). The theoretical limit of the maximum strain of this structure is 50%, which is sufficient for monitoring human signals^{4,20}. If more strain is applied, the contact area between the upper electrode and the ionic layer will decrease instead. It is worth mentioning that when excessive stretching occurs, the active material layer of the resistive strain sensor may be severely damaged, resulting in sensor failure. However, the active material layer of this GSS-designed capacitive sensor does not directly participate in the stretching, and the stretched part (Ecoflex) has a large stretching margin (>800%), which effectively avoids damage to the device caused by excessive stretching in practical applications.

Mechanism of the fringe field effect

The uniaxial tensile experimental data of the sensor designed by the GSS method are shown in Fig. 2a. It can be found that after 4% strain, the change of capacitance (ΔC) increased linearly as we expected. However, before the 4% strain, ΔC increases nonlinearly. We used a finite-element numerical method to explore the mechanism of this phenomenon. The electric field norm distribution in the upper electrode and ionic layer under small strain is shown in Fig. 2b. At the edge of the upper electrode, there is a large locally enhanced electric field, which is generated by the locally concentrated free electron density on the surface of the electrode. It originates from the migration of free electrons to the regions of the sharpest curvature on a charged metallic electrode, a consequence of electrostatic repulsion⁴². To estimate the impact of the locally enhanced electric field on the concentration of ions adsorbed on the surface, we used the Gouy–Chapman–Stern model to analyze the EDL capacitance. By coupling the Nernst–Planck and Poisson equations, we calculated the distribution of ions in the ionic layer. It can be seen that more ions gather at the edge of the upper electrode under the influence of the fringe field. Consequently, a large EDL capacitance is generated even if the contact area between the upper electrode and the ionic layer is very small (under a small strain). With the increase of strain, when the influence range of the locally enhanced electric field is not

enough to affect the formation of the EDL on the entire surface of the upper electrode, the subsequent increase of EDL capacitance is proportional to the subsequent increase in contact area as strain increases.

To address the issue of nonlinearity under small strain, we set the shape of the upper electrode as a trapezoid with an angle of θ (Fig. 2c). When the fringe field effect is not taken into account, the EDL capacitance is proportional to the contact area (S) between the upper electrode and the ionic layer, and the theoretical relationship between S and strain can be expressed as

$$S = \begin{cases} \frac{l^2 \tan \theta}{2} \cdot \varepsilon^2, & 0 < \varepsilon < \frac{w}{l \tan \theta} \\ \varepsilon \cdot lw - \frac{w^2}{2 \tan \theta}, & \frac{w}{l \tan \theta} \leq \varepsilon < 0.5 \end{cases} \quad (1)$$

where l is the length of the sensor, w is the width of the electrode. That is, the relationship between S and strain is a concave function under small strain. When the fringe field effect is taken into account, as actually tested, the relationship between ΔC and strain is a convex function for electrodes with $\theta = 90^\circ$. So the superposition of shape factor ($\theta < 90^\circ$) and fringe field factor provides the possibility to obtain linear sensors (Fig. 2d). The experiments also confirmed this conjecture. The nonlinearity of the electrical signal caused by the fringe field effect is gradually weakened with the decrease of θ (Fig. 2e). However, when θ is too small (for example, 79°), the influence of the shape factor on the capacitance change is too large, resulting in a concave function relationship between ΔC and strain, which also causes the electrical signal to be nonlinear. In the following experiments in this paper, electrodes with an angle of 87° were used. In addition, a chamfering procedure was carried out to lessen the fringe field effect and make the electrical signal more linear.

Sensing performance of the GSS-strain sensor

The sensitivity of the capacitive strain sensor is defined as $GF = \delta(\Delta C/C_0)/\delta\varepsilon$, where C and C_0 are the measured capacitance under stretching and the initial capacitance before applying strain (ε), respectively. For the sensor

designed by the GSS method, the EDL can be well used to increase the sensitivity. The GF of the GSS sensor studied here exhibits an extremely high value (9.1×10^6) over a broad sensing range. Most importantly, the electrical signal remains highly linear ($R^2 = 0.9997$) over the entire sensing range (Fig. 3a). Before strain is applied, the contact area of the ionic layer/electrode interface is substantially small, thus the initial capacitance C_0 is only several pF due to minimal EDL formation⁴³. With the increase of strain, the soft parts in the upper and lower gradient stiffness layers are deformed and elongated, resulting in the increase of the contact area between the electrode and the ionic layer, which significantly increases the EDL capacitance ($C \sim \mu\text{F}$), thus showing a great sensitivity⁴⁴. Furthermore, we prove from the opposite side that the change in capacitance is a result of the change in contact area (Supplementary Fig. 7). The reason why the EDL was not introduced into the conventional parallel-plate capacitive strain sensor to increase the sensitivity was that the stretching can only change the overall thickness and area of the sensor, which had little effect on the EDL capacitance located on the interface between electrodes and the ionic layer.

In addition, compared with resistive strain sensors, our capacitive sensor has an extremely fast dynamic response time of 17 ms when stretched to 0.5% strain (Fig. 3b). And it exhibits a low limit of detection (LOD) of 0.003% (Supplementary Fig. 8). The sensor also exhibits low sensitivity to strain rate²², as the change in capacitance remains constant at 7.2 μF ($\epsilon = 30\%$) for 0.25, 0.5, and 1 $\text{mm}\cdot\text{s}^{-1}$ tensile rates (Supplementary Fig. 9). Some existing resistive sensors exhibit hysteresis, which results in different measurements even at the same strain during loading and unloading. Hysteresis usually exists due to the viscoelastic nature of polymers as well as the interaction between the active material and polymers⁴⁵, which is very unfavorable in practical applications. In contrast, this capacitive sensor shows almost no hysteresis under loading/unloading cycles (Fig. 3c).

Water loss is a critical issue for most hydrogel-based strain sensors, which has a significant impact on the sensor's stability and sensing capabilities^{46,47}. Although the GSS-designed strain sensor also contains an ionic hydrogel, it is wrapped in upper and lower gradient stiffness layers, which prevents the hydrogel from being directly exposed to air and greatly reduces water loss (Supplementary Fig. 10), resulting in good performance

stability. We first evaluate its static response stability. The sensors are stretched by 10% and 40%, respectively, and hold for 60 min (Supplementary Fig. 11a). Capacitance remains almost unchanged in the air, demonstrating outstanding time-independent performance. And after a long period of stretch and release⁴⁸, the capacitance under different strains (0, 10, 20, 30, 40%) can all remain stable. The capacitance under the same strain remains unchanged (Supplementary Fig. 11b). We further evaluate its dynamic response stability. Under slow stretching ($0.5 \text{ mm}\cdot\text{s}^{-1}$), it maintains good stability under different strain cycles (Supplementary Fig. 12). Under fast stretching ($2 \text{ mm}\cdot\text{s}^{-1}$), the sensor still maintains outstanding performance stability in 2000 cycles with a peak strain of 40% (Fig. 3d). The sensor exhibits no signal drift or fluctuation which suggests that our device maintains a remarkable mechanical and sensing robustness without noticeable fatigue. As summarized in Fig. 3e, our GSS-designed iontronic capacitive strain sensor shows incomparably high sensitivity over a broad work range^{49–53}. The most important thing is that it not only has ultra-high sensitivity, but its electrical signal is also completely linear, outperforming existing strain sensors reported in the literature to the best of our knowledge.

In practical applications, the linearity of the electrical signal is essential. When installing the stretchable strain sensor onto a sensing target, such as human skin, the actual practical operation usually cannot ensure that the installation status of the sensor is strain-free. In this case, nonlinearity usually leads to large measurement errors²⁰. For a nonlinear strain sensor (Fig. 4a), assuming that the measured $\Delta R/R_0$ value is 'a' under the condition of pre-strain (the blue curve), while the measured strain value is the corresponding value of 'a' in the set relationship (the black curve) between resistance change and strain. This results in a difference between the measured value and the actual value, which severely affects the accuracy of the measurement. The nonlinearity of sensors makes the subsequent calibration process complex and challenging. In contrast, for a linear strain sensor, the measured value is consistent with the actual value regardless of whether there is a pre-strain, or even no matter how large the pre-strain is. A linear strain sensor can not only improve the measurement accuracy but also simplify wearable sensing systems without additional signal processing for the linear output, enabling device miniaturization and low power

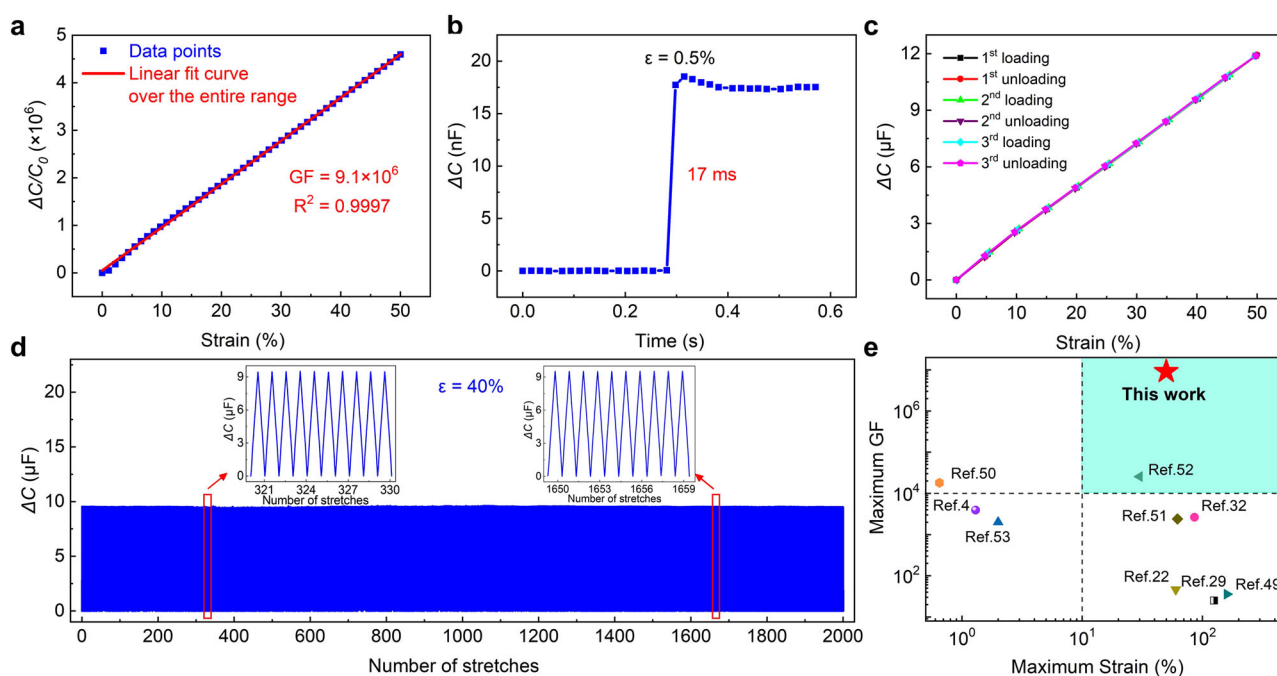


Fig. 3 | Sensing performance of the strain sensor designed by the GSS method. **a** Change of capacitance over the strain ranges up to 50%. **b** Response time. **c** Hysteresis of the capacitive-type strain sensor under three loading (50%/unloading) cycles. **d** Working stability tested over 2000 cycles at 40% strain. The inset

is an enlarged view of the change in capacitance of the sensor during cycles 320 to 330 and cycles 1650 to 1660. **e** Comparison of the sensitivity and sensing range of our capacitive-type strain sensor with existing sensors.

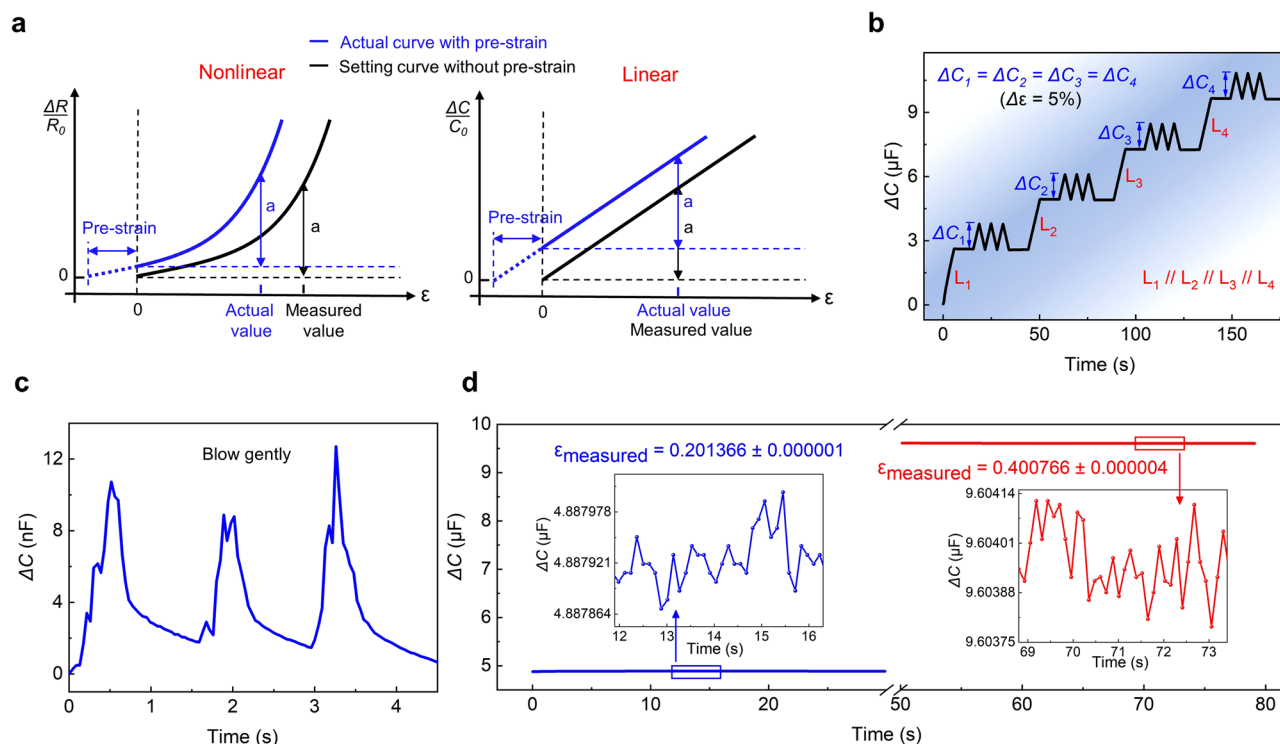


Fig. 4 | Outstanding linearity and sensitivity. **a** Influence of nonlinearity on the accuracy of strain sensor test results with pre-strain. **b** The change of capacitance under four step-by-step stretching (10%, 20%, 30%, 40%) and three stretching cycles

with an increment of 5%, respectively. **c** The small strain caused by gentle breathing can cause a significant change in the capacitance of the sensor. **d** The capacitance of the sensor at 20% and 40% strain and their enlarged diagrams.

consumption⁵⁴. Our GSS-designed strain sensor is almost ideal linear over the entire range ($R^2 = 0.9997$), which can perfectly meet this requirement. And since this linear property is gained through the design of the structure, rather than the design of the active material, this property has excellent robustness. The electrical signal remains linear even in the complex stretching process. We tested the capacitance change under four step-by-step stretching (10, 20, 30, 40%) and three stretching cycles with an increment of 5%, respectively (Fig. 4b). $L_1, L_2, L_3,$ and L_4 are the relationship curves of capacitance change and time in these four step-by-step stretching stages, respectively. The slopes of their fitting lines are all 0.4, which indicates that when the sensor is stretched in any initial state, the change of its capacitance shows the same linear relationship with the tensile strain. Also, the same strain increment ($\Delta\epsilon = 5\%$) results in the same capacitance change ($\Delta C = 1.2 \mu\text{F}$) at different initial strain states. These are the excellent characteristics that only linear sensors can have.

It is known that a high sensitivity indicates a low limit of detection and high resolution. For the GSS-designed sensor, the difference between the initial and maximum capacitance is very large. The change of capacitance spans seven orders of magnitude in the entire strain sensing range, which makes the sensor highly sensitive. It can even sense the tiny strain caused by a gentle breath on it (Fig. 4c and Supplementary Video 1). In addition, systematic errors in the measurement of electrical signals during practical applications are inevitable. We tested the capacitance value of the GSS-designed sensor under 20% and 40% strain, respectively (Fig. 4d). Although the electrical signal appears to be a straight line, the enlarged diagram reveals that the capacitance value has fluctuated, indicating that the measured strain value also fluctuates accordingly. If the fluctuation range of the measured strain value is too large, the test's accuracy will be severely affected. The huge electrical signal variation span of this highly sensitive sensor makes the fluctuation range of the strain value extremely narrow, thus greatly improving the accuracy of the test. We substituted the measured capacitance value into the capacitance-strain linear fitting curve obtained in Fig. 3a, and calculated that the strain fluctuation ranges measured by the sensor are 0.201366 ± 0.000001 and 0.400766 ± 0.000004 under 20% and 40% strain,

respectively, indicating a very narrow range of test inaccuracy. However, it should be noted that in practice the absolute value of the measurement error of an LCR meter increases with the measurement capacitance. The sensitivity increased by reducing the initial capacitance and increasing the final capacitance is only a theoretical value. Current test instruments have difficulty achieving the expected theoretical values, especially in the large-strain range.

This sensor is able to accurately monitor a variety of human signals in practical applications (Fig. 5a), from subtle expression changes (Fig. 5b, c) to large-scale bending of arms and knees (Fig. 5d–f). Moreover, different frequencies of stimuli for everyday life can be monitored steadily and accurately, including fast coffee shaking and slow stir-frying (Fig. 5e). It is also worth mentioning that transparent flexible sensors can also be prepared by using transparent electrodes to meet the needs of some specific application scenarios (Supplementary Fig. 13).

In summary, the EDL is introduced into the design of capacitive strain sensors to improve the sensitivity by controlling the distribution of the locally enhanced electric field and the heterogeneous deformation of the substrate. The limitation of the low sensitivity of capacitive strain sensors is fundamentally addressed while maintaining full range linearity, together with almost no hysteresis. The GSS-designed sensor also has the advantages of over-stretching protection and structural robustness, leading to the real potential for practical application. We believe that the GSS method provides a general design strategy for the significant improvement of the performance of other types of sensors and the development of new fields of flexible electronics.

Methods

Mechanical finite-element analysis

Since the PDMS part and PVC layer deformed only in a small strain range, they were set as linear elastomers. The Young's modulus of the PDMS⁵⁵ and PVC were set to 1.98 and 3500 MPa, respectively, and the Poisson's ratios were set to 0.45 and 0.38, respectively. The Ecoflex part was modeled as a hyperelastic material⁵⁶. The third-order reduced polynomial model (Yeoh

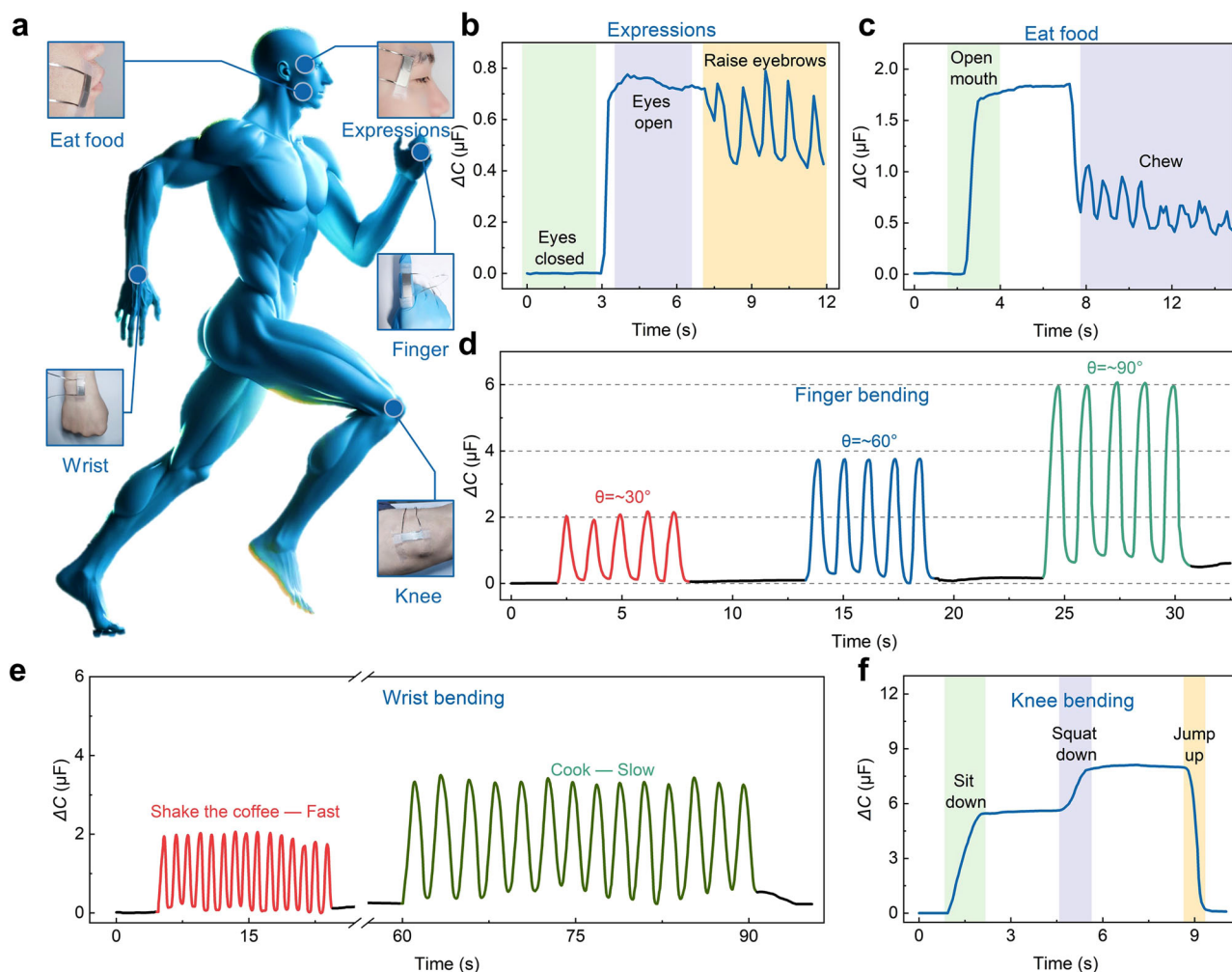


Fig. 5 | Applications of the GSS-designed sensor for strain detection. **a** Overview of the sensing locations. **b**, **c** Monitoring of **b** expressions and **c** people’s eating process. **d** Monitoring of different degrees of finger bending. **e** The scenes of people shaking coffee quickly and stirring food slowly in daily life were simulated to evaluate

the monitoring performance of the sensor for stimulation frequency. **f** The performance of the sensor for monitoring large-strain signals was evaluated by fixing the sensor on the knee and having the experimenter sit down, squat down, and then quickly jump up.

model) was used for Ecoflex with parameter values $N = 3$, $C_{10} = 5072 \text{ J}\cdot\text{m}^{-3}$, $C_{20} = -331 \text{ J}\cdot\text{m}^{-3}$, and $C_{30} = -15 \text{ J}\cdot\text{m}^{-3}$. The contact between the PDMS and Ecoflex parts was defined as bonding.

Electrical finite-element analysis

The electric double layer was modeled using the Gouy–Chapman–Stern model, which consists of a Helmholtz layer and a diffusion layer. The Nernst–Planck equation and the Poisson equation are combined to describe the ion mass transfer and current density distribution. The coupling form is also known as the Nernst–Planck–Poisson (NPP) equation. These coupled equations are extremely nonlinear and convergence is difficult. Therefore, some simplifications were made to the model under the premise of not affecting the exploration of the mechanism of the fringe field. The two-dimensional model was built to represent the three-dimensional ionic layer and electrodes used in this work. The voltage on the electrode was set to $-\sin(2\pi 1000[\text{Hz}]t) \text{ V}$. Although the voltage was transient, according to the physical nature of capacitance, the capacitance was constant when the contact area between the upper electrode and the ionic layer was constant. Therefore, in this paper, we choose a time of 0.51 ms for analysis. And the concentration of ions was set to $10^{-7} \text{ mol}/\text{m}^3$. Triangular meshes were used for all simulations. The meshes were set to be denser on the surface of the ionic layer to increase simulation accuracy.

Preparation of PAM/LiCl ionic layers as the dielectric

The PAM hydrogel was synthesized by free-radical polymerization using ammonium persulfate as an initiator. First, 8.34 g of acrylamide, 1.586 g of sodium acrylate, and 0.115 g of N,N’-methylenebisacrylamide was dissolved into 100 mL deionized water, followed by stirring for 30 min until they dissolved completely (solution A). Then 1.11 g of ammonium persulfate was dissolved into 10 g of deionized water (solution B). 2.54 g of LiCl was dissolved into 10 mL of solution A in an ice-water bath. After that, this pre-gel solution mixed with 15 μL of N,N,N’,N’-tetramethylethylenediamine, and 50 μL of solution B was cast on the electrode to form the ionic layer.

Preparation of gradient stiffness layers and assembly of strain sensors

First, the half area of a 0.15 mm thick flexible PVC film was covered, and only the other half area was treated with plasma for 30 min. The PDMS (the mass ratio of monomer and cross-linker was 10:2) was then cast onto the plasma-treated area and cured at 70° for 20 min. Then Ecoflex-0030 was cast on the untreated PVC area, the Ecoflex part and PDMS part were fused and cured at 75° for 12 h. The thickness of the PDMS part and Ecoflex part was 0.5 mm. So far, the hard PDMS/PVC part and the soft Ecoflex part formed a gradient stiffness substrate. Then a 0.02 mm thick flexible titanium sheet was stuck on the other side of the PVC layer corresponding to the Ecoflex part as the electrode. Alternatively, a layer of Au could be deposited on the

substrate by magnetron sputtering as an electrode. A 0.5 mm thick PAM/LiCl ionic layer was further cast on the electrode. Finally, a PDMS/PVC-Ecoflex gradient stiffness layer with only the electrode and another gradient stiffness layer covered with the ionic layer on the electrode was assembled head to tail to form a capacitive-type strain sensor. The Ecoflex part and PDMS part of the upper and lower gradient stiffness layers at both ends were cured and bonded together with several additional drops of PDMS. Optionally, a small amount of lubricant (0.1 g talc, Aladdin) could also be dropped into the gap between the Ecoflex part and the PVC layer, so that the Ecoflex part could slide smoothly on the PVC layer. The size of the strain sensor was set to 30×10 mm.

Measurements and characterization

The capacitance was measured by using an LCR meter (E4980A, KEY-SIGHT). All capacitance signals tests were performed at 1 kHz, except that the response time test was performed at 10 kHz to make the LCR meter have a lower sampling interval. Mechanical tests were carried out by an instrument equipped with two tension clamps and a 100 N load cell. The microstructures of the transparent electrodes were characterized by using the scanning electron microscope (Supra55).

Data availability

The authors declare that the data supporting the findings of this study are available within the paper and its supplementary information files.

Received: 28 July 2023; Accepted: 24 February 2024;

Published online: 07 March 2024

References

- Maurya, D. et al. 3D printed graphene-based self-powered strain sensors for smart tires in autonomous vehicles. *Nat. Commun.* **11**, 5392 (2020).
- Zheng, L. et al. Conductance-stable liquid metal sheath-core microfibers for stretchy smart fabrics and self-powered sensing. *Sci. Adv.* **7**, eabg4041 (2021).
- Zhang, T. et al. Self-powered stretchable sensor arrays exhibiting magnetoelasticity for real-time human-machine interaction. *Adv. Mater.* **35**, e2203786 (2022).
- Yan, W. et al. Giant gauge factor of Van der Waals material based strain sensors. *Nat. Commun.* **12**, 2018 (2021).
- Zhao, Y. et al. Bioinspired multifunctional photonic-electronic smart skin for ultrasensitive health monitoring, for visual and self-powered sensing. *Adv. Mater.* **33**, e2102332 (2021).
- Jiang, Z. et al. A 1.3-micrometre-thick elastic conductor for seamless on-skin and implantable sensors. *Nat. Electron.* **5**, 784–793 (2022).
- Cui, X. et al. Flexible pressure sensors via engineering microstructures for wearable human-machine interaction and health monitoring applications. *iScience* **25**, 104148 (2022).
- Yu, Z. & Wu, P. Water-resistant ionogel electrode with tailorable mechanical properties for aquatic ambulatory physiological signal monitoring. *Adv. Funct. Mater.* **31**, 2107226 (2021).
- Ahn, S. et al. Wearable multimode sensors with amplified piezoelectricity due to the multi local strain using 3D textile structure for detecting human body signals. *Nano Energy* **74**, 104932 (2020).
- Yu, Q. et al. Highly sensitive strain sensors based on piezotronic tunneling junction. *Nat. Commun.* **13**, 778 (2022).
- Cui, X. et al. Stretchable strain sensors with dentate groove structure for enhanced sensing recoverability. *Compos. Part B Eng.* **211**, 108641 (2021).
- Li, J., Li, S. & Su, Y. Stretchable strain sensors based on deterministic-contact-resistance braided structures with high performance and capability of continuous production. *Adv. Funct. Mater.* **32**, 2208216 (2022).
- Li, G. et al. Three-dimensional flexible electronics using solidified liquid metal with regulated plasticity. *Nat. Electron.* **6**, 154–163 (2023).
- Qin, J. et al. Flexible and stretchable capacitive sensors with different microstructures. *Adv. Mater.* **33**, e2008267 (2021).
- Lee, J. et al. Stretchable and suturable fibre sensors for wireless monitoring of connective tissue strain. *Nat. Electron.* **4**, 291–301 (2021).
- Chen, L. et al. The piezotronic effect in InGaN/GaN quantum-well based microwire for ultrasensitive strain sensor. *Nano Energy* **72**, 104660 (2020).
- Cai, Y. et al. Extraordinarily stretchable all-carbon collaborative nanoarchitectures for epidermal sensors. *Adv. Mater.* **29**, 1606411 (2017).
- Yang, Y., Shi, L., Cao, Z., Wang, R. & Sun, J. Strain sensors with a high sensitivity and a wide sensing range based on a $\text{Ti}_3\text{C}_2\text{T}_x$ (MXene) nanoparticle–nanosheet hybrid network. *Adv. Funct. Mater.* **29**, 1807882 (2019).
- Hui, Y. et al. Three-dimensional printing of soft hydrogel electronics. *Nat. Electron.* **5**, 893–903 (2022).
- Li, S. et al. Contact-resistance-free stretchable strain sensors with high repeatability and linearity. *ACS Nano* **16**, 541–553 (2022).
- Amjadi, M., Kyung, K.-U., Park, I. & Sitti, M. Stretchable, skin-mountable, and wearable strain sensors and their potential applications: a review. *Adv. Funct. Mater.* **26**, 1678–1698 (2016).
- Wang, Y. et al. A durable nanomesh on-skin strain gauge for natural skin motion monitoring with minimum mechanical constraints. *Sci. Adv.* **6**, eabb7043 (2020).
- Boutry, C. M. et al. A stretchable and biodegradable strain and pressure sensor for orthopaedic application. *Nat. Electron.* **1**, 314–321 (2018).
- Liu, Z. et al. Highly breathable and stretchable strain sensors with insensitive response to pressure and bending. *Adv. Funct. Mater.* **31**, 2007622 (2021).
- Azadi, S. et al. Biocompatible and highly stretchable PVA/AgNWs hydrogel strain sensors for human motion detection. *Adv. Mater. Technol.* **5**, 2000426 (2020).
- Pan, S. et al. Mechanocombinatorially screening sensitivity of stretchable strain sensors. *Adv. Mater.* **31**, e1903130 (2019).
- Kim, S. H. et al. Ultrastretchable conductor fabricated on skin-like hydrogel-elastomer hybrid substrates for skin electronics. *Adv. Mater.* **30**, e1800109 (2018).
- Matsuhisa, N. et al. Printable elastic conductors with a high conductivity for electronic textile applications. *Nat. Commun.* **6**, 7461 (2015).
- Liu, Z. et al. Surface strain redistribution on structured microfibers to enhance sensitivity of fiber-shaped stretchable strain sensors. *Adv. Mater.* **30**, 1704229 (2018).
- Xue, F. et al. An ultra-broad-range pressure sensor based on a gradient stiffness design. *Mater. Horiz.* **8**, 2260–2272 (2021).
- Jiang, Y. et al. Auxetic mechanical metamaterials to enhance sensitivity of stretchable strain sensors. *Adv. Mater.* **30**, e1706589 (2018).
- Feng, B. et al. Nacre-inspired, liquid metal-based ultrasensitive electronic skin by spatially regulated cracking strategy. *Adv. Funct. Mater.* **363**, 2102359 (2021).
- Zhou, H. et al. Robust and sensitive pressure/strain sensors from solution processable composite hydrogels enhanced by hollow-structured conducting polymers. *Chem. Eng. J.* **403**, 126307 (2021).
- Jiang, P.-P., Qin, H., Dai, J., Yu, S.-H. & Cong, H.-P. Ultrastretchable and self-healing conductors with double dynamic network for omni-healable capacitive strain sensors. *Nano Lett.* **22**, 1433–1442 (2022).
- Shintake, J., Nagai, T. & Ogishima, K. Sensitivity improvement of highly stretchable capacitive strain sensors by hierarchical auxetic structures. *Front. Robot. AI* **6**, 127 (2019).
- Nur, R. et al. A highly sensitive capacitive-type strain sensor using wrinkled ultrathin gold films. *Nano Lett.* **18**, 5610–5617 (2018).

37. Nesser, H. & Lubineau, G. Achieving super sensitivity in capacitive strain sensing by electrode fragmentation. *ACS Appl. Mater. Interfaces* **13**, 36062–36070 (2021).
38. Huang, X. et al. High-stretchability and low-hysteresis strain sensors using origami-inspired 3D mesostructures. *Sci. Adv.* **9**, eadh9799 (2023).
39. Mo, F. et al. A highly stable and durable capacitive strain sensor based on dynamically super-tough hydro/organo-gels. *Adv. Funct. Mater.* **31**, 2010830 (2021).
40. Okuda, T., Kurose, K., Nishijima, W. & Okada, M. Separation of polyvinyl chloride from plastic mixture by froth flotation after surface modification with ozone. *Ozone Sci. Eng.* **29**, 373–377 (2007).
41. Qiu, Z. et al. Ionic skin with biomimetic dielectric layer templated from *Calathea Zebrina* leaf. *Adv. Funct. Mater.* **28**, 1802343 (2018).
42. Liu, M. et al. Enhanced electrocatalytic CO₂ reduction via field-induced reagent concentration. *Nature* **537**, 382–386 (2016).
43. Bai, N. et al. Graded intrafillable architecture-based iontronic pressure sensor with ultra-broad-range high sensitivity. *Nat. Commun.* **11**, 209 (2020).
44. Li, H. et al. Ultraflexible and tailorable all-solid-state supercapacitors using polyacrylamide-based hydrogel electrolyte with high ionic conductivity. *Nanoscale* **9**, 18474–18481 (2017).
45. Amjadi, M., Pichitpajongkit, A., Lee, S., Ryu, S. & Park, I. Highly stretchable and sensitive strain sensor based on silver nanowire-elastomer nanocomposite. *ACS Nano* **8**, 5154–5163 (2014).
46. Wen, J. et al. Multifunctional ionic skin with sensing, UV-filtering, water-retaining, and anti-freezing capabilities. *Adv. Funct. Mater.* **31**, 2011176 (2021).
47. Zhang, Y.-Z. et al. MXenes stretch hydrogel sensor performance to new limits. *Sci. Adv.* **4**, eaat0098 (2018).
48. Zhang, M. et al. Carbonized cotton fabric for high-performance wearable strain sensors. *Adv. Funct. Mater.* **27**, 1604795 (2017).
49. Tan, C. et al. A high performance wearable strain sensor with advanced thermal management for motion monitoring. *Nat. Commun.* **11**, 3530 (2020).
50. Liu, L. et al. Bioinspired, omnidirectional, and hypersensitive flexible strain sensors. *Adv. Mater.* **34**, e2200823 (2022).
51. Shi, X., Liu, S., Sun, Y., Liang, J. & Chen, Y. Lowering internal friction of 0D-1D-2D ternary nanocomposite-based strain sensor by fullerene to boost the sensing performance. *Adv. Funct. Mater.* **28**, 1800850 (2018).
52. Hu, T. et al. Omnidirectional configuration of stretchable strain sensor enabled by the strain engineering with chiral auxetic metamaterial. *ACS Nano* **17**, 22035–22045 (2023).
53. Kang, D. et al. Ultrasensitive mechanical crack-based sensor inspired by the spider sensory system. *Nature* **516**, 222–226 (2014).
54. Lee, Y. et al. Flexible ferroelectric sensors with ultrahigh pressure sensitivity and linear response over exceptionally broad pressure range. *ACS Nano* **12**, 4045–4054 (2018).
55. Elsayed, Y. et al. Finite element analysis and design optimization of a pneumatically actuating silicone module for robotic surgery applications. *Soft Robot.* **1**, 255–262 (2014).
56. Naserifar, N., LeDuc, P. R. & Fedder, G. K. Material gradients in stretchable substrates toward integrated electronic functionality. *Adv. Mater.* **28**, 3584–3591 (2016).

Acknowledgements

This work was supported by the Fundamental Research Funds for the Central Universities, Heilongjiang Provincial Natural Science Foundation of China (Grant No. YQ2020E009).

Author contributions

F.X. conceived the ideas and designed the experiments under the guidance of Q.P., X.Z., and X.H. F.X., H.Z., L.X. and X.Z. performed experiments and analysis. F.X., Z.T. and P.L. performed computer simulations. F.X. and R.D. co-wrote the manuscript. All the authors discussed the results and commented on the manuscript.

Competing interests

The authors declare no competing interests.

Additional information

Supplementary information The online version contains supplementary material available at <https://doi.org/10.1038/s41528-024-00301-7>.

Correspondence and requests for materials should be addressed to Qingyu Peng, Xinxing Zhang or Xiaodong He.

Reprints and permissions information is available at <http://www.nature.com/reprints>

Publisher's note Springer Nature remains neutral with regard to jurisdictional claims in published maps and institutional affiliations.

Open Access This article is licensed under a Creative Commons Attribution 4.0 International License, which permits use, sharing, adaptation, distribution and reproduction in any medium or format, as long as you give appropriate credit to the original author(s) and the source, provide a link to the Creative Commons licence, and indicate if changes were made. The images or other third party material in this article are included in the article's Creative Commons licence, unless indicated otherwise in a credit line to the material. If material is not included in the article's Creative Commons licence and your intended use is not permitted by statutory regulation or exceeds the permitted use, you will need to obtain permission directly from the copyright holder. To view a copy of this licence, visit <http://creativecommons.org/licenses/by/4.0/>.

© The Author(s) 2024